

Supplementary Materials

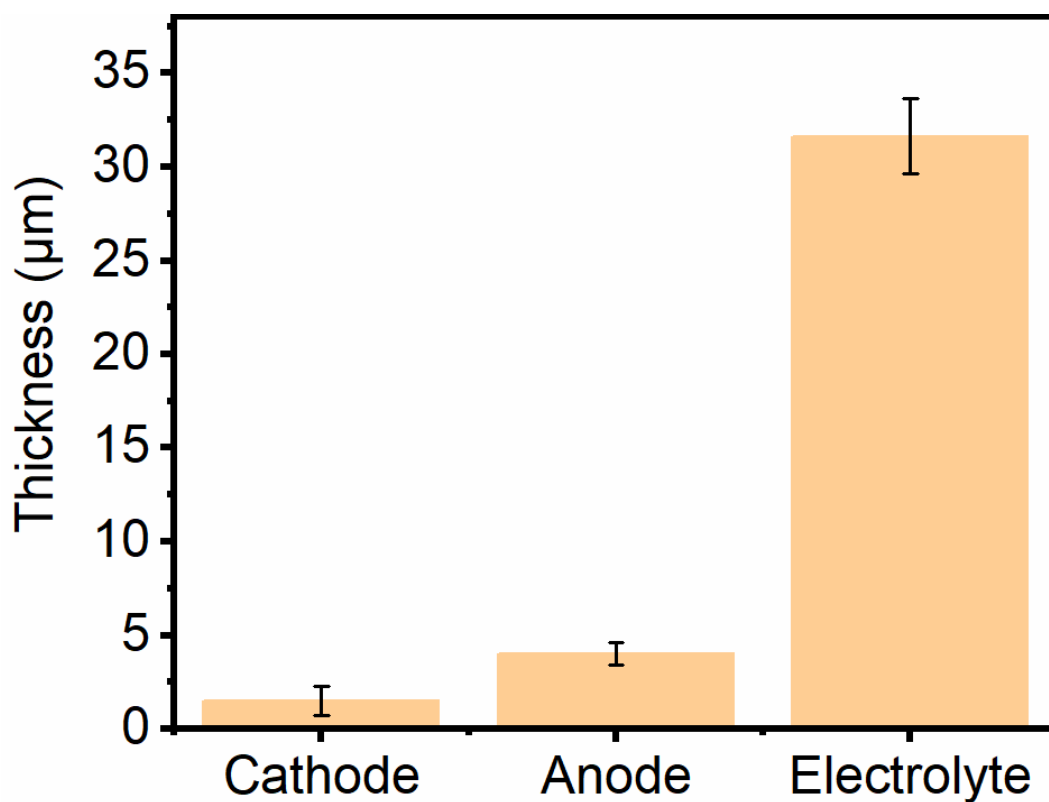


Fig. S1. Thickness of MnOx/PPy cathode, zinc anode and photoluminescent gelatin based electrolyte.

Figure S1 exhibits the thickness of the cathode, anode and electrolyte layer in the μ ZMB.

The thickness of MnOx/PPy is around 1.5 μ m, while the thickness of the zinc anode is around 4.02 μ m. For the photoluminescent gelatin based electrolyte layer is around 31.64 μ m.

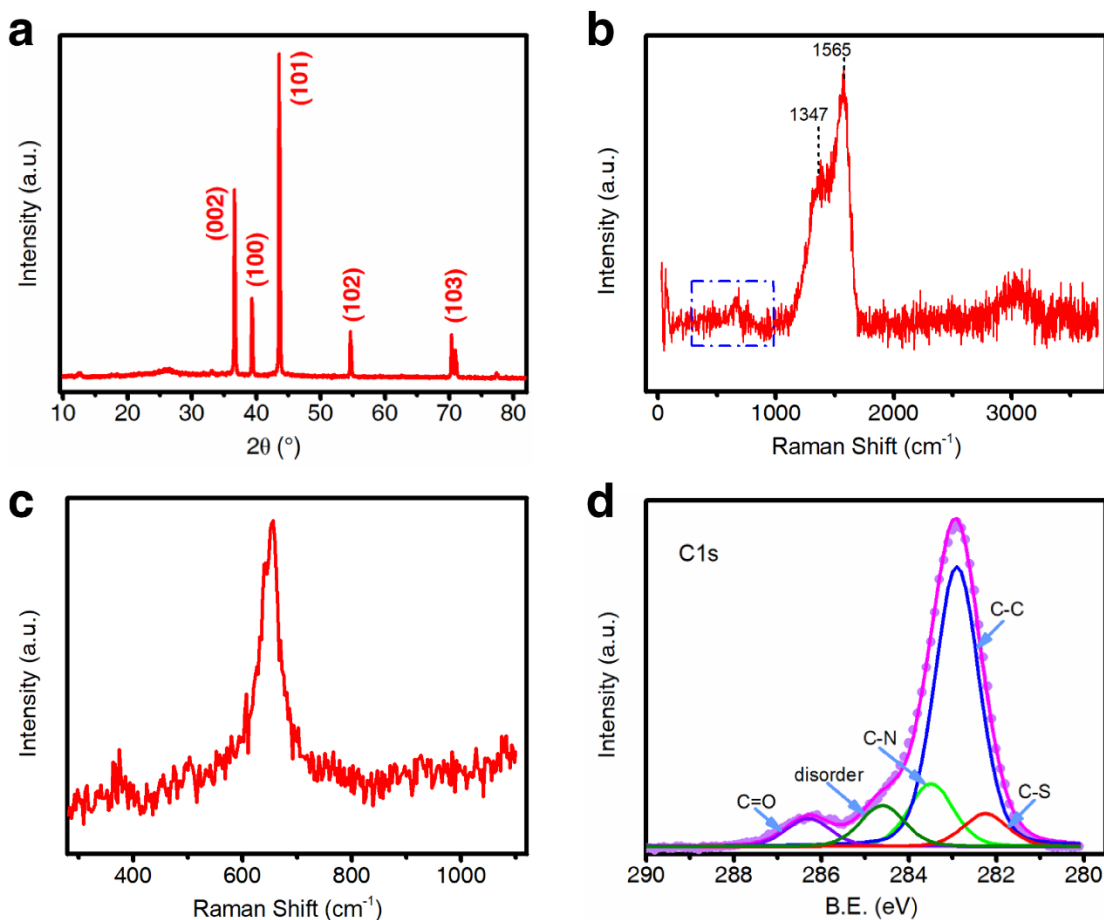


Fig. S2. Material characterization of electrode materials. (a) The XRD pattern of the electrodeposited zinc. (b) The Raman spectrum of the electrodeposited MnO_x/PPy in the range of 0 – 3800 cm^{-1} and (c) 280 – 1020 cm^{-1} . (d) The XPS C 1s core spectrum of the electrodeposited MnO_x/PPy .

Fig. S2a displays the XRD pattern of the electrodeposited zinc. Sharp peaks are observed, indicating its high crystallinity, which can be indexed as the reflexes of zinc (JCPDS: 65-3358). Fig. S2b shows the Raman spectrum of the electrodeposited MnO_x/PPy . Two peaks centered at 1347 and 1565 cm^{-1} are assigned to the polypyrrole. In addition, a weak peak before 1000 cm^{-1} is observed in the wide-range Raman spectrum. The spectrum between 300 to 1100 cm^{-1} is shown in Fig. S2c, displaying a sharp peak centered at 650 cm^{-1} , which is assigned to the electrodeposited MnO_x . Accordingly, the Raman spectrum reveals the

blend structure of the MnO_x and PPy. Fig. S2d shows the C 1s core spectrum of the electrodeposited MnO_x/PPy measured by the XPS. The C 1s core spectrum can be deconvoluted into five peaks: α carbons (C–N), β carbons (C–C), carbonyl carbons (C=O), carbon atoms bonded with sulfur (C–S) and disordered carbons. Among these, carbonyl carbons are formed by the reaction with water molecules during electrochemical polymerization process. Carbon atoms bonded with sulfur are assigned to the doped PPy induced by the sulfur containing dopant (pTSA). The disordered carbons are attributed to the interaction between PPy and MnO_x during layer-by-layer depositing process. This further reveals the strong contact between PPy and MnO_x .

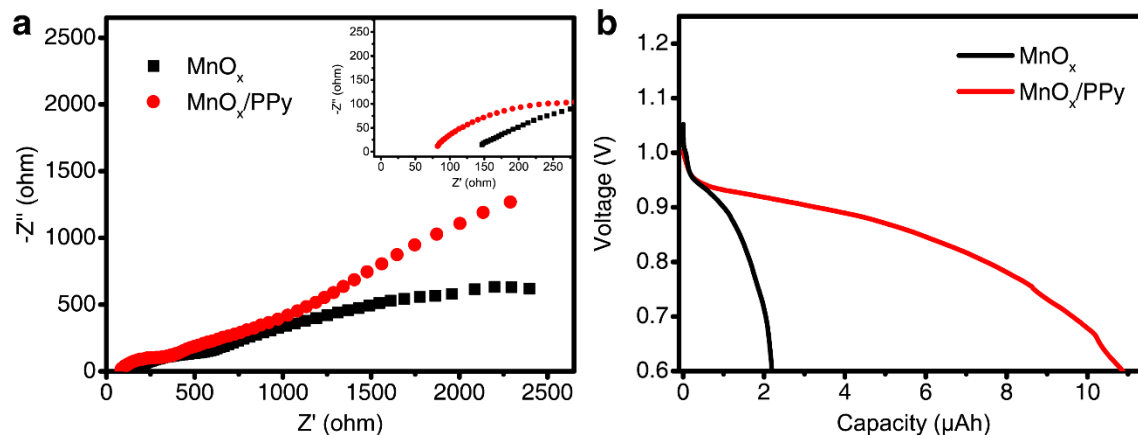


Fig. S3. Comparison of the performance between MnO_x and MnO_x/PPy based cathodes. (a) Nyquist plots and (b) galvanostatic discharge curves (current: 0.5 mA) of MnO_x based μZMB and MnO_x/PPy based μZMB . The electrolyte utilized in tests is 1M aqueous ZnSO_4 .

Fig. S3a shows the impedance spectra of MnO_x based μZMB and MnO_x/PPy based μZMB .

The MnO_x/PPy based μZMB experiences faster electrochemical kinetic as the slope of the Nyquist plot in the low frequency region is larger than that of the MnO_x based μZMB .

Moreover, the magnified plot in the high frequency region (inset in Fig. S3a) shows that the first intersection point with the real axis of MnO_x/PPy based μZMB is smaller than that of the MnO_x based μZMB , indicating a lower bulk resistance of MnO_x/PPy . Owing to the faster kinetic and lower bulk resistance of MnO_x/PPy , the MnO_x/PPy based μZMB delivers a capacity of 11 μAh , which is more than five times of the capacity delivered by the MnO_x based μZMB (2.1 μAh) (Fig. S3b).

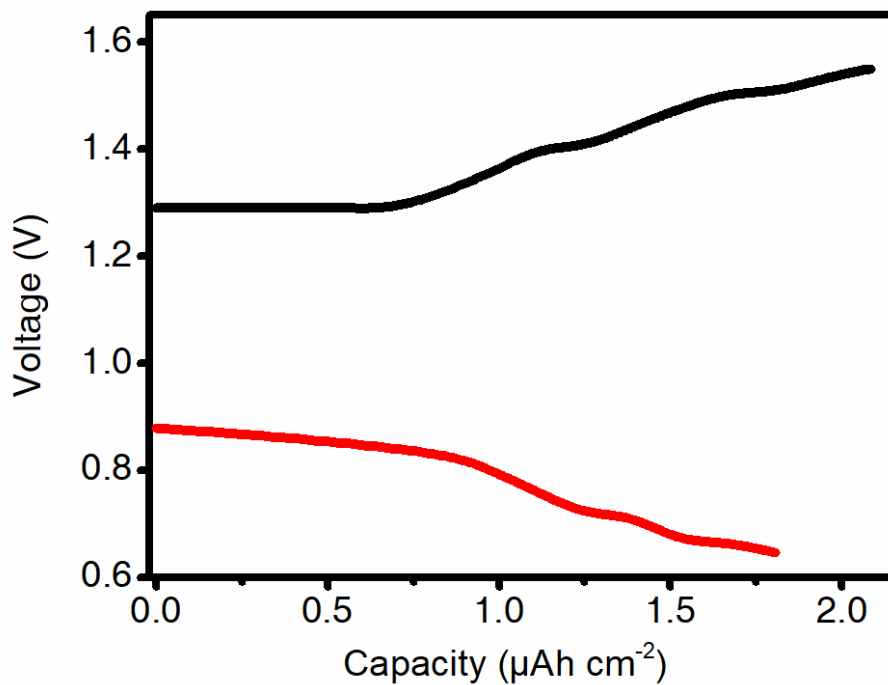


Fig. S4. Charge/discharge profile of the PPy versus zinc anode.

Fig. S4 shows the charge/discharge profile of the PPy versus zinc anode. The capacity achieved under 0.2 mA cm^{-2} is less than $2.0 \mu\text{Ah cm}^{-2}$, which is less 2% of the capacity achieved by the MnO_x/PPy based cathode. Therefore, the contribution of the capacity from PPy can be neglected.

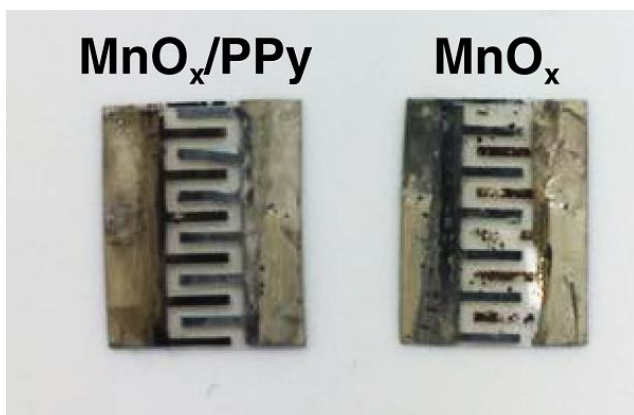


Fig. S5. Digital photograph of the MnO_x/PPy and MnO_x microbatteries after 5 charge/discharge cycles.

Fig. S5 displays the MnO_x/PPy and MnO_x microbatteries after 5 charge/discharge cycles.

The contact between MnO_x/PPy and the ITO substrate is strong (left), while large amounts of MnO_x peels off from the ITO substrate (right). With a MnO_x peeling off from the substrate, short circuit may be caused as it will create a path between the anode and cathode.

The addition of PPy strengthens the contact with the ITO substrate, thus providing stable performance.

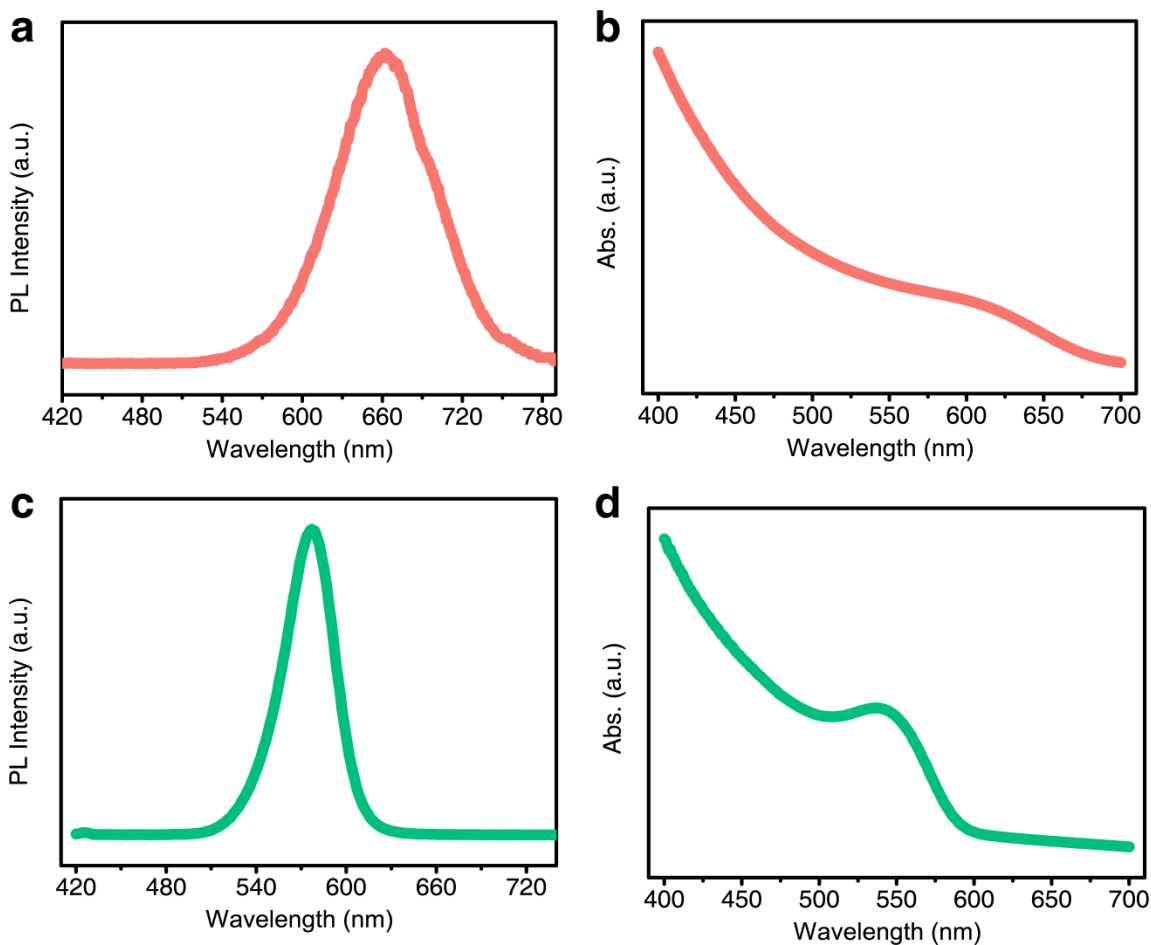


Fig. S6. PL and absorption spectra of CdTe QDs. (a) The PL and (b) absorption spectrum of CdTe QDs with red emission. (c) The PL and (d) absorption spectrum of CdTe QDs with green emission.

Fig. S6 displays PL emission spectrum and UV–vis absorption of the CdTe QDs dissolved in water. A red emission peak centered at 662 nm is recognized in the PL emission (Fig. S6a). A continuous and broad absorption (from 400 to 650 nm), with a peak at 625 nm is observed for the UV-vis absorption (Fig. S6b). Similarly, a sharp green emission peak centered at 560 nm is recognized in the PL (Fig. S6c). A continuous and broad absorption (from 400 to 575 nm), with a well-resolved peak at 550 nm is observed for the UV-vis absorption (Fig. S6d).

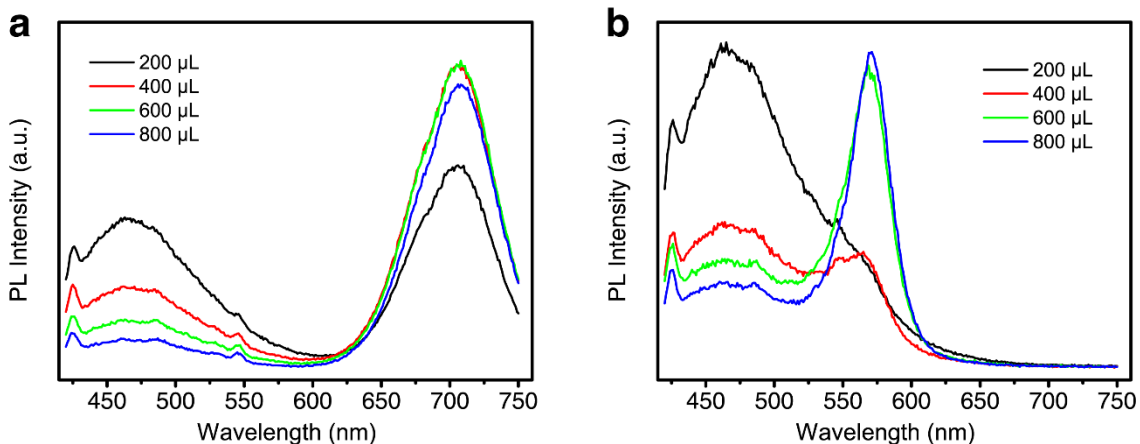


Fig. S7. Relationship between the PL intensity and the added amount of CdTe QDs in the photoluminescent electrolyte for the (a) red-emitting and (b) green-emitting samples. Volumes provided on the frames stay for the amount of QDs solutions added into a 5 mL gelatin based electrolyte.

Fig. S7 displays the PL spectra of the photoluminescent electrolyte upon adding different amounts of the red (Fig. S7a) and green (Fig. S7b) CdTe QD solutions. For both cases, the contribution of blue emission originating from gelatin is strong for the case of addition of 200 μL QD solution. With the increasing amount of the QDs, the blue emission is suppressed while the red or the green emission becomes stronger. The optimum amount of CdTe QDs with red emission added into the gelatin based electrolyte is 600 μL , because further addition of QDs doesn't result in a higher PL intensity (Fig. S7a). Also for the green-emitting electrolyte, although 800 μL of added QDs leads to a slightly higher PL intensity, it the optimum amount of the added QDs is set to be 600 μL (Fig. S7b).

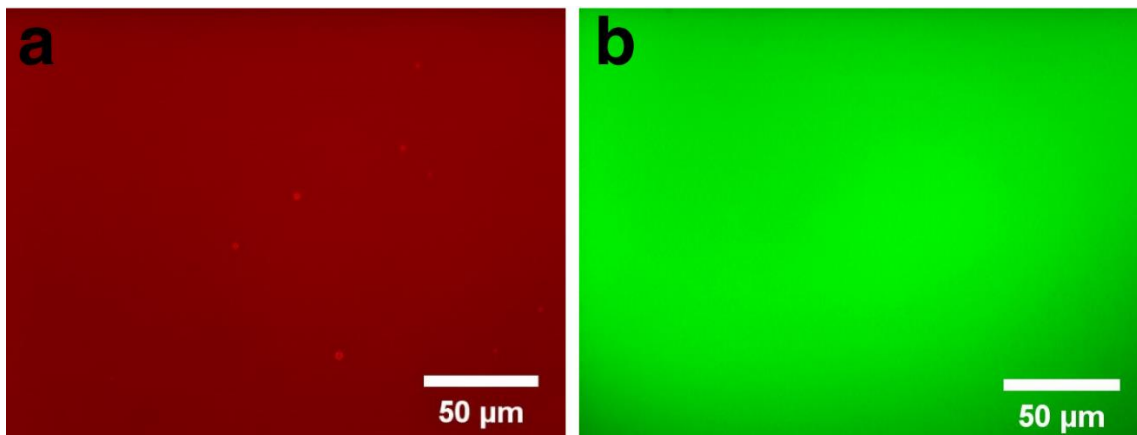


Fig. S8. The fluorescence micrographs of photoluminescent gelatin-based electrolyte with red (a) and green (b) emission.

Fig. S8 shows the fluorescence micrographs of photoluminescent gelatin-based electrolyte. Uniform distribution of CdTe QDs in electrolyte can be observed for the electrolyte with either red or green emission. The uniform distribution of CdTe QDs will render the homogeneous emission of light.

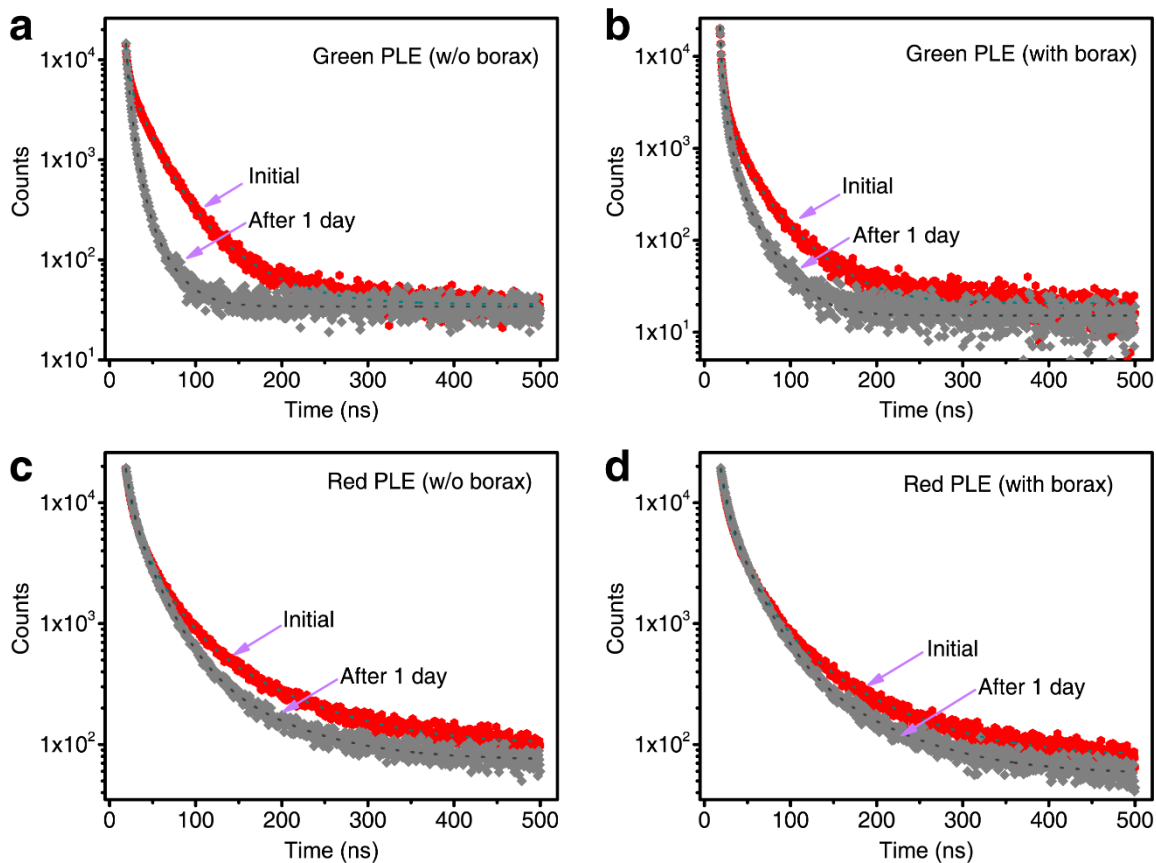


Fig. S9. PL decay curves of the photoluminescent electrolytes for the freshly prepared (“initial”) green-emitting CdTe QD containing sample and after 1-day aging (a) without borax and (b) with borax, alongside with the red-emitting CdTe QD containing samples (c) without borax and (d) with borax.

Fig. S9 displays the PL decay curves of green and red emitting CdTe QDs in the green- and red-emitting electrolytes before and after 1-day aging with and without addition of borax. After 1-day aging, a decrease of the PL lifetime is observed for both green and red emitting QDs, which can be attributed to eliminating the surface trap states and defects during aging process. The recorded PL decay curves have been fitted by three exponential functions, with the data for PL lifetimes summarized in Table S1.

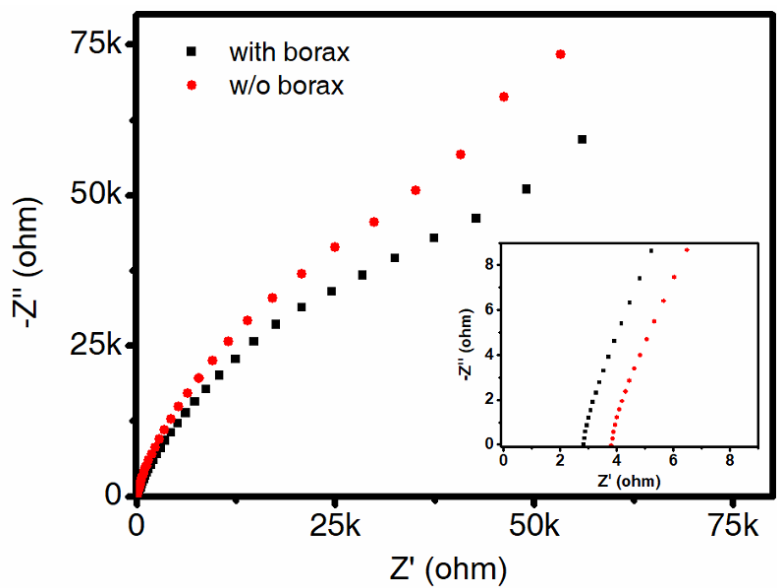


Fig. S10. The Nyquist plot of the gelatin based electrolyte with and without borax. The inset is the magnification of the range between 0-9 Ω .

Fig. S10 shows the impedance spectra of the gelatin based electrolyte with and without borax. Two pieces of stainless steel sheets are utilized as electrodes. In the middle frequency range, the gelatin based electrolyte with borax exhibits faster charge transference than that of the electrolyte without borax. This indicates that the addition of borax enhances the mobility of zinc ions in the electrolyte. Furthermore, the first intersection point with the real axis for the gelatin based electrolyte with borax is by 27% smaller than that of the electrolyte without borax. Considering the identical dimension and thickness of the two electrolytes, the ionic conductivity of gelatin based electrolyte with borax can be thus considered 27% higher than that without borax.

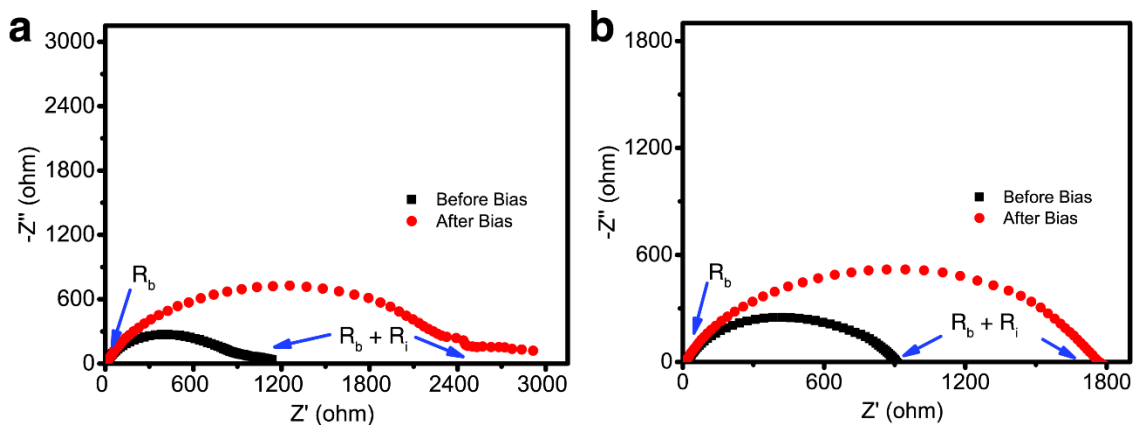


Fig. S11. Investigation of the zinc ion transference number. The Nyquist plot of the gelatin based electrolyte (a) with borax and (b) without borax. The gelatin based electrolyte is sandwiched by two zinc foils. The potential bias applied on the gelatin based electrolyte is 50 mV.

To investigate the zinc ion transference number, gelatin based electrolyte with (Fig. S10a) or without (Fig. S10b) borax is sandwiched by two pieces of zinc foils during the impedance test. The black curves in both figures are measured at initial state. The red curves are measured after applying a small voltage bias (50 mV) on the cell for 1500 s. For the both impedance spectra, the first intersection point with real axis is originated from the bulk resistance (R_b). The second intersection point is the sum of the bulk and interfacial resistance (R_b+R_i). Therefore, the interfacial resistance (R_i) is obtained by subtracting value of R_b from R_b+R_i .

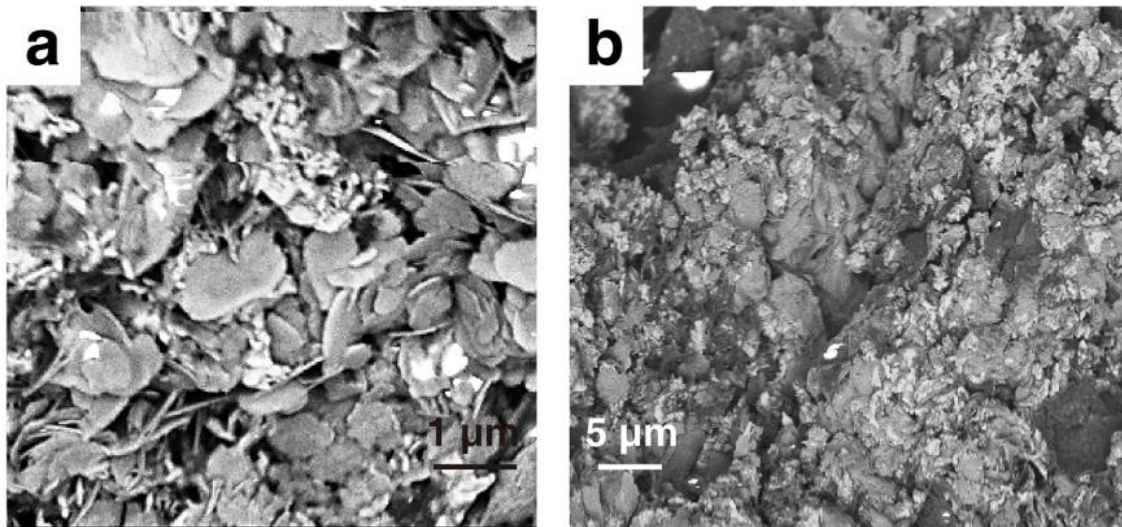


Fig. S12. The SEM images of the zinc anode (a) and MnO_x/PPy cathode (b) after 200 charge/discharge cycles.

Figure S12 shows the SEM image of the anode and cathode after cycling test. In Fig. S12a, zinc nanosheets network can still be observed, indicating the excellent cycling stability of zinc anode. For the MnO_x/PPy cathode, the morphology evolves from the nanoporous network to a nanocluster network after 200 charge/discharge cycles. However, this nanocluster network still benefits the penetration of the electrolyte. Therefore, the excellent cycling stability of MnO_x/PPy based microbattery was obtained, as shown in Figure 3d.

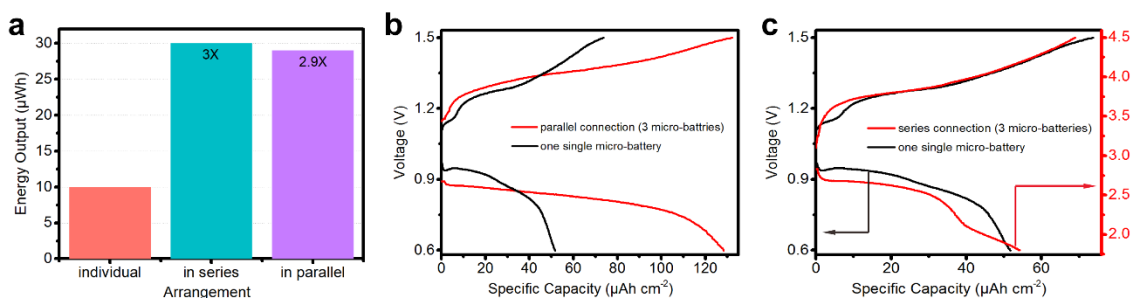


Fig. S13. Performance of microbatteries in series and parallel connection. (a) The comparison of energy output delivered by single μ ZMB and three μ ZMBs in series and parallel connection. (b) Galvanostatic charge/discharge curves of single μ ZMB and three μ ZMBs in parallel connection. (c) Galvanostatic charge/discharge curves of single μ ZMB and three μ ZMBs in series connection.

Fig. S13a shows the energy output of different μ ZMB units. One single μ ZMB delivers the energy of 10 μ Wh. After connecting three μ ZMBs in parallel and series arrangement, the energy output triples, reaching about 30 μ Wh. When μ ZMBs are in parallel connection, the operational voltage is almost identical to that of a single μ ZMB, while the capacity triples (Fig. S13b). For the μ ZMBs in series connection, the operational voltage triples (Fig. S13c). Therefore, the operational voltage μ ZMB unit can be tuned toward the target application by connecting μ ZMBs in series arrangement.

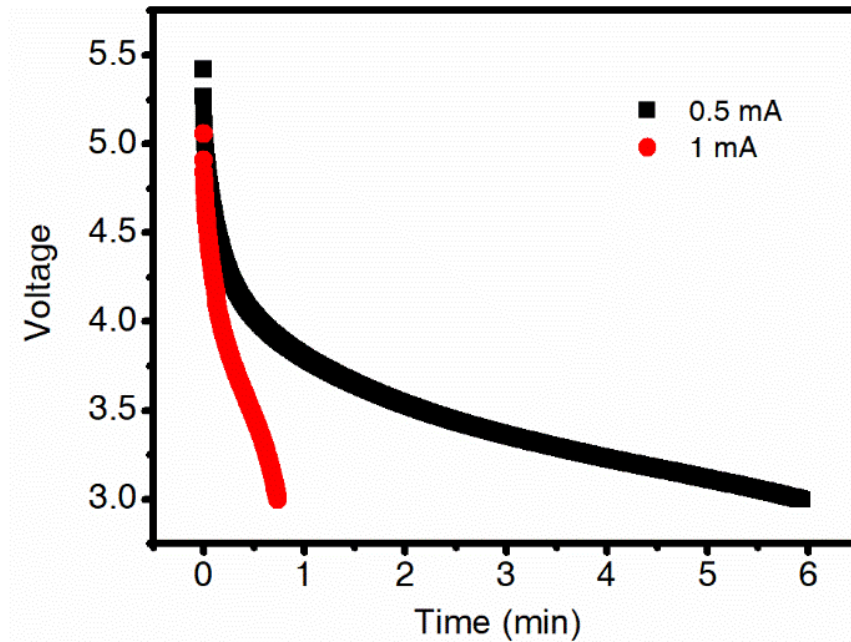


Fig. S14. The discharge profile of the μ ZMB array under the current of 0.5 mA and 1 mA. As a practical power source for electronic devices, the cut-off voltage is set as 3.0V for the discharging test. It is obvious that the μ ZMB array can last for 6 min under the discharge current of 0.5 mA. With the current increases to 1 mA, the μ ZMB array still can last for around 1 min.

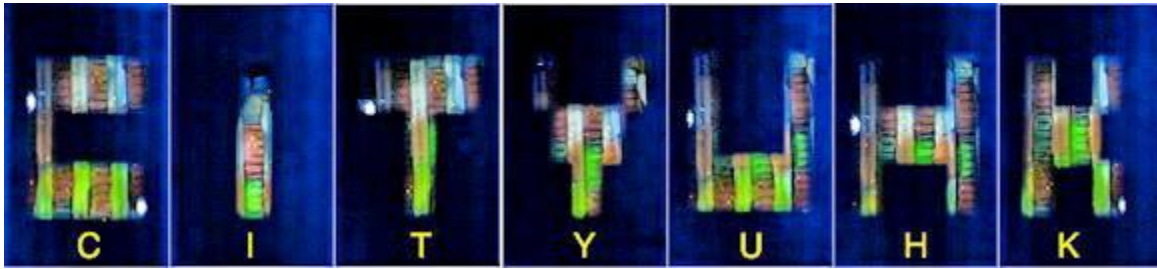


Fig. S15. Digital photographs of the simulation of full-color display with different light shields.

Simulation of a full-color display with different light shields is provided in Fig. S15. Upon rapid changing these light shields, dynamic full-color display is simulated as demonstrated in the Video S1.

Table S1. PL lifetimes (τ_{1-3} , ns) and fractions of the emission intensity (f_{1-3} , %) obtained from the fitting of experimental PL decays (see Figure S6) by three-exponential functions for the green and red photoluminescent electrolytes with freshly-added (“initial”) CdTe QDs and those experiencing 1-day aging or adding borax. Average PL lifetime τ_a (ns) for all cases are also provided.

Sample		Component, τ /ns (f/%)			τ_a
		1	2	3	
Green electrolyte (with borax)	Initial	1.8 (29.8)	11.5 (39.4)	40.6(30.8)	17.6
	After 1 day	1.6 (38.1)	6.8(41.2)	26.0 (20.7)	8.8
Green electrolyte (w/o borax)	Initial	1.8 (14.3)	16.8(50.1)	42.9(35.5)	23.9
	After 1 day	2.0 (30.5)	6.2 (53.4)	21.5 (16.1)	7.3
Red electrolyte (with borax)	Initial	5.6 (16.8)	23.7 (51.3)	83.5 (31.9)	39.7
	After 1 day	6.6 (20.4)	25.0 (60.1)	84.2 (19.5)	32.8
Red electrolyte (w/o borax)	Initial	5.6 (17.5)	24.9 (50.0)	89.3 (32.5)	42.5
	After 1 day	6.5 (22.4)	24.0 (58.9)	81.0 (18.7)	30.7

Table S1 shows the PL lifetimes and the fractions of each PL lifetime components for the photoluminescent electrolyte samples with/without borax, freshly mixed with CdTe QDs

and after 1-day aging. For all samples, a decrease of the average PL lifetime is observed after 1-day aging. The decrease of PL lifetime (69%, from 23.9 to 7.3 ns) for the green emitting QDs is higher than that for the red emitting QDs (28%, from 42.5 to 30.7 ns). This is because green emitting QDs possess higher surface-to-volume ratio caused by their relatively smaller size, which results in the lower stability compared with red emitting QDs. After adding borax, only 50% and 17% decrease of the PL lifetime is observed for the green and red emitting QDs after 1-day aging, respectively. This indicates that addition of borax protects the surface of QDs, ensuring their higher stability¹⁻⁴.

Table S2. Comparison of electrochemical performance of energy storage devices in micro-scale.

Material	Device type	Specific capacity	Volume energy density	ref.
TiO ₂ tube	LIB, half cell	370 $\mu\text{Ah cm}^{-2}$	—	5
TiO ₂ /Pt tube	LIB, half cell	150 $\mu\text{Ah cm}^{-2}$	—	6
LiMnO ₂ /Ni-Sn	LIB, full cell	—	15 mWh cm^{-3}	7
PANI/Ni-Sn	LIB, full cell	100 $\mu\text{Ah cm}^{-2}$	—	8
V ₂ O ₅	LIB, half cell	86 $\mu\text{Ah cm}^{-2}$	—	9
LTO/LFP	LIB, full cell	1.5 mAh cm^{-2} (160 mAh g^{-1})	—	10
LMO/Ni-Sn	LIB, full cell	—	4.5 mWh cm^{-3}	11
LFP/LTO	LIB, full cell	160 mAh g^{-1}	—	12
LiTiOS/Si	LIB, full cell	130 $\mu\text{Ah cm}^{-2}$	—	13
MnO_x/PPy/Zn	ZIB, full cell	110 $\mu\text{Ah cm}^{-2}$ (327 mAh g^{-1} cathode)	21 mWh cm^{-3}	our work

References

- 1 Adam, M., Erdem, T., Stachowski, G. M., Soran-Erdem, Z., Lox, J. F., Bauer, C., Poppe, J., Demir, H. V., Gaponik, N. & Eychmuller, A. Implementation of High-Quality Warm-White Light-Emitting Diodes by a Model-Experimental Feedback Approach Using Quantum Dot-Salt Mixed Crystals. *ACS Appl. Mater. Interfaces* **7**, 23364-23371 (2015).
- 2 Adam, M., Gaponik, N., Eychmuller, A., Erdem, T., Soran-Erdem, Z. & Demir, H. V. Colloidal Nanocrystals Embedded in Macrocrystals: Methods and Applications. *J. Phys. Chem. Lett.*, 4117-4123 (2016).
- 3 Otto, T., Muller, M., Mundra, P., Lesnyak, V., Demir, H. V., Gaponik, N. & Eychmuller, A. Colloidal nanocrystals embedded in macrocrystals: robustness, photostability, and color purity. *Nano Lett.* **12**, 5348-5354 (2012).
- 4 Wang, X. Y., Qu, L. H., Zhang, J. Y., Peng, X. G. & Xiao, M. Surface-related emission in highly luminescent CdSe quantum dots. *Nano Lett.* **3**, 1103-1106 (2003).
- 5 Letiche, M., Eustache, E., Freixas, J., Demortiere, A., De Andrade, V., Morgenroth, L., Tilmant, P., Vaurette, F., Troadec, D., Roussel, P., Brousse, T. & Lethien, C. Atomic Layer Deposition of Functional Layers for on Chip 3D Li-Ion All Solid State Microbattery. *Adv. Energy Mater.* **7**, 1601402 (2017).
- 6 Eustache, E., Tilmant, P., Morgenroth, L., Roussel, P., Patriarche, G., Troadec, D., Rolland, N., Brousse, T. & Lethien, C. Silicon-Microtube Scaffold Decorated with Anatase TiO₂ as a Negative Electrode for a 3D Lithium-Ion Microbattery. *Adv. Energy Mater.* **4**, 1301612 (2014).
- 7 Pikul, J. H., Zhang, H. G., Cho, J., Braun, P. V. & King, W. P. High-power lithium ion microbatteries from interdigitated three-dimensional bicontinuous nanoporous electrodes. *Nat. Commun.* **4**, 1732 (2013).
- 8 Gowda, S. R., Reddy, A. L. L. M., Zhan, X. B. & Ajayan, P. M. Building Energy Storage Device on a Single Nanowire. *Nano Lett.* **11**, 3329-3333 (2011).
- 9 Gerasopoulos, K., Pomerantseva, E., McCarthy, M., Brown, A., Wang, C. S., Culver, J. & Ghodssi, R. Hierarchical Three-Dimensional Microbattery Electrodes Combining Bottom-Up Self-Assembly and Top-Down Micromachining. *ACS Nano* **6**, 6422-6432 (2012).
- 10 Sun, K., Wei, T. S., Ahn, B. Y., Seo, J. Y., Dillon, S. J. & Lewis, J. A. 3D Printing of Interdigitated Li-Ion Microbattery Architectures. *Adv. Mater.* **25**, 4539-4543 (2013).
- 11 Ning, H. L., Pikul, J. H., Zhang, R. Y., Li, X. J., Xu, S., Wang, J. J., Rogers, J. A., King, W. P. & Braun, P. V. Holographic patterning of high-performance on-chip 3D lithium-ion microbatteries. *P. Natl. Acad. Sci. USA* **112**, 6573-6578 (2015).
- 12 Fu, K., Wang, Y. B., Yan, C. Y., Yao, Y. G., Chen, Y. A., Dai, J. Q., Lacey, S., Wang, Y. B., Wan, J. Y., Li, T., Wang, Z. Y., Xu, Y. & Hu, L. B. Graphene Oxide-Based

- Electrode Inks for 3D-Printed Lithium-Ion Batteries. *Adv. Mater.* **28**, 2587 (2016).
- 13 Le Cras, F., Pecquenard, B., Dubois, V., Phan, V. P. & Guy-Bouyssou, D. All-Solid-State Lithium-Ion Microbatteries Using Silicon Nanofilm Anodes: High Performance and Memory Effect. *Adv. Energy Mater.* **5**, 1501061 (2015).